GeoConvention 2014
FOCUS
adapt
refine
sustain

Reverse time migration of prestack elastic data

R. Ferner, Department of Physics, University of Alberta, ferner@ualberta.ca
M. D. Sacchi, Department of Physics, University of Alberta

Summary

Formulations of finite-difference solutions to the elastic wave-equation are well documented in geophysical literature. These finite-difference solutions model elastic wave propagation within a medium on a discrete grid. Elastic wave propagation modelling makes possible the ability to extrapolate vector wave-fields forwards and backwards through time. A major application of this is a depth imaging technique known as reverse time migration. Elastic reverse time migration extrapolates source and receiver wave-fields in combination with an imaging condition; generating depth images of subsurface impedance contrasts for both primary and converted seismic phases. The technique utilizes two-dimensional isotropic elastic prestack data, and is capable of handling steeply dipping complex structure. We will examine the effectiveness of the method applying it to a faulted model synthetic data set and analyzing the results.

Introduction

The first reverse time migration algorithms outlined by Baysal et al. (1983) and Whitmore (1983) operate on poststack seismic data and assume the seismic wave propagation to be acoustic. Chang and McMechan (1987) formulate a two way elastic wave-equation reverse time migration for prestack data, where the imaging condition incorporates ray tracing to calculate the image time. The migration algorithm of Botelho and Stoffa (1991) also uses an elastic-wave equation for computing image times and receiver extrapolation; however, does not consider generating separate images for primary and converted seismic phases. More contemporary techniques propose generating independent images for primary and converted phases via decomposing the elastic wave-field into scalar and vector potentials (Sun and McMechan, 2001; Yan and Sava, 2008). Although different all these reverse time migration algorithms can be simplified into two steps, a wave-field extrapolation, and an imaging condition (Sava and Fomel, 2006). The wave-field extrapolation requires a method to model seismic wave propagation forwards and backwards through time. The imaging condition then exploits our physical understanding of wave-field scattering to locate subsurface impedance contrasts. Thus, the accuracy of our imaging algorithm depends largely on our ability to realistically model seismic wave propagation.

Finite-difference modelling

The derivation of Madariaga (1976), describes elastodynamic equations as a first-order hyperbolic system of particle velocity and stress. This system of partial differential equations shown in 1 defines (v_x, v_z) as horizontal and vertical particle velocities, (T_{xx}, T_{zz}, T_{xz}) as the horizontal, vertical and shear stresses, (λ, μ) as the Lamé parameters and ρ as density. The compressional and shear velocities (V_p, V_s) can be expressed as the Lamé parameters and density. Setting μ equal to zero reduces the system to the acoustic case explained in detail by Virieux (1984), allowing accurate solid liquid interface modelling.

$$\begin{aligned}
\frac{\partial v_x}{\partial t} &= \frac{1}{\rho}\left(\frac{\partial T_{xx}}{\partial x} + \frac{\partial T_{xz}}{\partial z}\right) & \frac{\partial v_z}{\partial t} &= \frac{1}{\rho}\left(\frac{\partial T_{zz}}{\partial z} + \frac{\partial T_{xz}}{\partial x}\right) \\
\frac{\partial T_{xx}}{\partial t} &= (\lambda + 2\mu)\frac{\partial v_x}{\partial x} + \lambda\frac{\partial v_z}{\partial z} & \frac{\partial T_{zz}}{\partial t} &= (\lambda + 2\mu)\frac{\partial v_z}{\partial z} + \lambda\frac{\partial v_x}{\partial x} \\
\frac{\partial T_{xz}}{\partial t} &= \mu\left(\frac{\partial v_x}{\partial z} + \frac{\partial v_z}{\partial x}\right)
\end{aligned} \tag{1}$$

Virieux (1986) outlines a detailed staggered grid finite-difference scheme to solve this system of equations. The staggered grid method discretizes the system of equations 1, where the components are staggered both spatially and temporally. This is demonstrated by equation 2 and Figure 1 for the horizontal particle velocity component v_x from equations 1. It can be seen how spacial finite-difference derivative approximations of stresses (T_{xx}, T_{xz}) at time t and the horizontal particle velocity value v_x at time $t - \frac{1}{2}$ update the system for the horizontal particle velocity value v_x at time $t + \frac{1}{2}$. Although the forward process is outlined, this algorithm can be run forwards or backward in time. Depicted is the second-order finite-difference stencil in both space and time $O(\Delta t^2, x^2)$. To improve the stability of the Madariaga-Virieux algorithm the order of the finite-difference derivative approximations can be increased spatially and temporally (Bayliss et al., 1986; Levander, 1988). For this paper stencils are second-order in time and fourth-order in space $O(\Delta t^2, x^4)$.

$$v_{x(i,j)}^{t+\frac{1}{2}} = v_{x(i,j)}^{t-\frac{1}{2}} + \frac{1}{\rho}_{(i,j)} \frac{\Delta t}{\Delta x}(T_{xx(i-\frac{1}{2},j)}^{t} - T_{xx(i+\frac{1}{2},j)}^{t}) + \frac{1}{\rho}_{(i,j)} \frac{\Delta t}{\Delta z}(T_{xz(i,j-\frac{1}{2})}^{t} - T_{xz(i,j+\frac{1}{2})}^{t}) \tag{2}$$

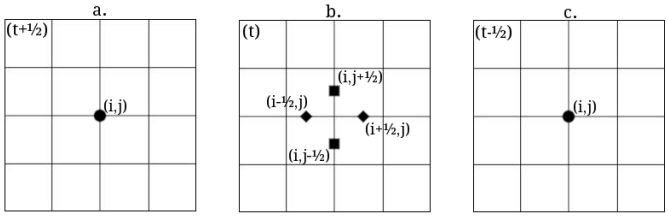

Figure 1 *Visual representation of equation 2 on standard staggered grid. Note the grid is staggered both temporally and Spatially. a.) Horizontal particle velocity (circle) at time* $t + \frac{1}{2}$*. b.) Normal Horizontal Stress (diamond) and Shear Stress (square) at time* t*. c.) Horizontal particle velocity (circle) at time* $t - \frac{1}{2}$*.*

The propagation of the elastic wave-field into unbounded model edges will generate undesirable boundary reflections. Chew and Liu (1996) demonstrate that a perfectly matched layer can exist within elastic solids that completely absorbs and annihilates elastic waves that propagate within the layer. The method splits each wave-field component into directional derivative auxiliary equations, parallel and perpendicular to the boundary. The splitting procedure is delineated in equation 3 for the horizontal particle velocity component v_x from equations 1 (the superscript denotes the directional derivative). Collino and Tsogka (2001) introduce perfect matching layer dampening parameters for the Madariaga-Virieux finite-difference scheme. Shown in equation 4 the dampening parameters are derived from the compressional velocity V_p, thickness of boundary N, and a theoretical reflection coefficient R. These dampening parameters are then applied to the auxiliary equation perpendicular to the boundary as it propagates into the perfectly matched layer.

$$\frac{\partial v_x^x}{\partial t} + D(x)v_x^x = \frac{1}{\rho}\frac{\partial T_{xx}}{\partial x} \quad and, \quad \frac{\partial v_x^z}{\partial t} + D(z)v_x^z = \frac{1}{\rho}\frac{\partial T_{xz}}{\partial z} \tag{3}$$

$$D(x) = d_x^{max}\left(\frac{x}{N\Delta x}\right)^2 \quad where, \quad d_x^{max} = log\left(\frac{1}{R}\right)\frac{3V_p}{2N\Delta x}$$

$$D(z) = d_z^{max}\left(\frac{z}{N\Delta z}\right)^2 \quad where, \quad d_z^{max} = log\left(\frac{1}{R}\right)\frac{3V_p}{2N\Delta z} \tag{4}$$

Recording each time step of the elastic wave-field propagation at discrete receiver locations in the model (r_x, r_z), we can generate realistic synthetic multi-component seismograms free from numerical grid dispersion and boundary artifacts. This elastic finite-difference scheme will act as the engine of the reverse time migration algorithm.

Cross-correlation imaging condition

For a given shot profile k we can visualize seismic recordings as a series of snapshots of the seismic wave-field restricted to only the receiver locations $d_k(x = r_x, z = r_z, t)$. Other than the direct arrival, all recorded energy is associated with subsurface impedance contrasts scattering source energy back to the receivers. We can extrapolate our restricted view of the wave-field back through time via finite-difference. If we have an accurate velocity model, the back propagated wave-field will be properly positioned in the subsurface model (x, z) at each time step. This is referred to as the receiver side wave-field:

$$d_k(x = r_x, z = r_z, t) \xrightarrow[extrapolation]{finite-difference} R_k(x, z, t)$$

Similarly, if we have prior knowledge of the position (s_x, s_z) and temporal shape of the source function (seismic wavelet) $s_k(x = s_x, z = s_z, t)$, we can extrapolate energy of the source wave-field forward through time. This is referred to as the source side wave-field:

$$s_k(x = s_x, z = s_z, t) \xrightarrow[extrapolation]{finite-difference} S_k(x, z, t)$$

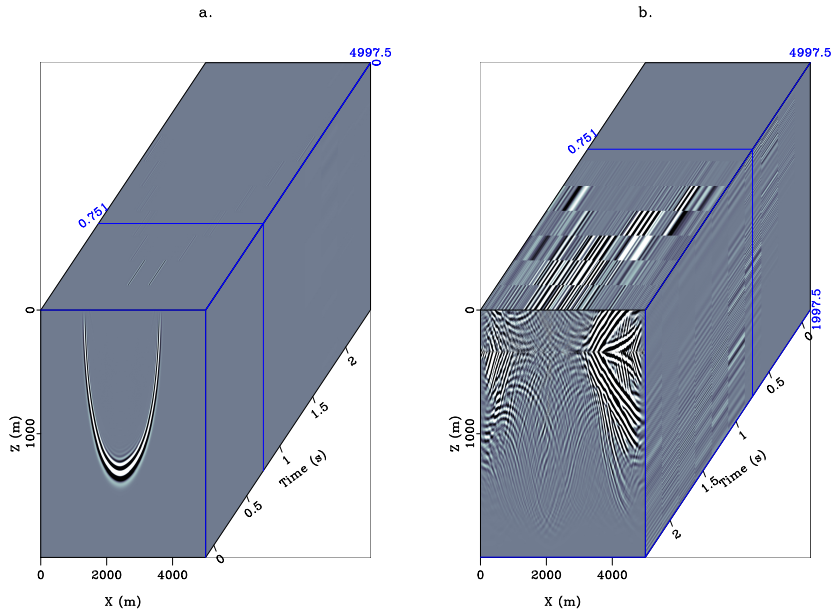

Figure 2 *Visual representation of snapshot cubes for a single shot k. a.) The source side wave-field $S_k(x, z, t)$ with the $0.751\,s$ snapshot shown. b.) The Receiver side wave-field $R_k(x, z, t)$ with the $0.751\,s$ snapshot shown.*

If source side and receiver side energy exist at the same position in the subsurface at time step t, this reveals a subsurface reflector where source energy scattering has occurred. This is the concept of the cross-correlation imaging condition (Claerbout, 1985). The mathematical representation is delineated by $P_k(x, z)$, in equation 5, as the zero lag cross-correlation of the source and receiver side snapshot cubes. Stacking each partial image $P_k(x, z)$ generates the final image $F(x, z)$.

$$P_k(x, z) = \sum_t S_k(x, z, t) R_k(x, z, t) \tag{5}$$
$$F(x, z) = \sum_k P_k(x, z)$$

When imaging using scalar wave-fields the cross-correlation imaging condition becomes straight forward. However, when imaging with vector wave-fields each source side and receiver side wave-field is composed of multiple components adding complexity to the imaging condition.

Imaging with compressional and shear modes

A corollary of Helmholtz Theorem states that for any divergence free vector field Ψ and curl free scalar field Φ there exists a unique vector field $\mathbf{V}$ such that:

$$\nabla \cdot \mathbf{V} = \Phi \quad and, \quad \nabla \times \mathbf{V} = \Psi \tag{6}$$

In two-dimensional isotropic media the compressional wave mode $P_w(x,z,t)$ corresponds purely to volumetric perturbations (curl free). Similarly, the shear wave mode $S_w(x,z,t)$ corresponds purely to shearing/shape perturbations (divergence free). Therefore, the isotropic elastic wave-field $\mathbf{U}(\mathbf{x},\mathbf{z},\mathbf{t})$ composed of compressional and shear wave modes can be described as a vector field with a prescribed divergence and curl where:

$$\nabla \cdot \mathbf{U}(\mathbf{x},\mathbf{z},\mathbf{t}) = P_w(x,z,t) \quad and, \quad \nabla \times \mathbf{U}(\mathbf{x},\mathbf{z},\mathbf{t}) = S_w(x,z,t) \tag{7}$$

Dellinger and Etgen (1990) exploit this property of the elasodynamic equations in isotropic media, separating finite-difference modelled elastic wave-fields into compressional and shear modes via divergence and curl operators. Applying wave mode separation to the source and receiver snapshot cubes, Yan and Sava (2008) formulate an expanded cross-correlation imaging condition for vector wave-fields. This is shown in equation 8 where the superscripts on the source side and receiver side snapshot cubes denotes the corresponding wave mode.

$$\begin{aligned} P_k^{PP}(x,z) &= \sum_t S_k^{P_w}(x,z,t) R_k^{P_w}(x,z,t) \quad and, \quad P_k^{PS}(x,z) = \sum_t S_k^{P_w}(x,z,t) R_k^{S_w}(x,z,t) \\ F^{PP}(x,z) &= \sum_k P_k^{PP}(x,z) \quad and, \quad F^{PS}(x,z) = \sum_k P_k^{PS}(x,z) \end{aligned} \tag{8}$$

This imaging condition has a clear physical interpretation, as cross-correlation of a source side and a receiver side compressional mode gives an image of the migrated primary seismic phases $P_K^{PP}(x,z)$. Similarly, cross-correlation of a source side compressional mode with a receiver side shear mode gives an image of the converted seismic phases $P_K^{PS}(x,z)$.

Examples

The velocity model shown in Figure 3 a.) was used to conduct a synthetic seismic survey. The survey was designed as an ocean bottom node survey with 500 receivers placed on the ocean floor ($Z = 400\,m$) at a $10\,m$ spacing. 64 shots were fired $10\,m$ below the sea surface, with a regular shot interval of $75\,m$. The top boundary of the model was set to be a perfect matching layer such that no free surface multiples were propagated. The recorded wave-field for the $X = 3000\,m$ shot is shown in Figure 4. The recorded data with the direct and scholte waves removed was then back propagated from the receivers through the smooth velocity model shown in Figure 3 b.). For each back propagated shot k the snapshots of the wave-field were split into compressional and shear modes via divergence and curl operations producing $R_k^{P_w}(x,z), R_k^{S_w}(x,z)$. Concurrently, the source function for each shot k was forward propagated through the smooth velocity model producing $S_k^{P_w}(x,z)$. Note no shear mode for the source side wave-field as a pressure source was implemented. The vector cross-correlation imaging condition was then applied producing partial images $P_k^{PP}(x,z), P_k^{PS}(x,z)$. The partial images were then bandpass filtered and the $P_k^{PS}(x,z)$ images corrected for negative offset polarity reversal. Stacking the partial images and muting above the first reflector produced the final images shown in Figure 5. Note the algorithms ability to resolve the complex notch structure in the bottom three layers.

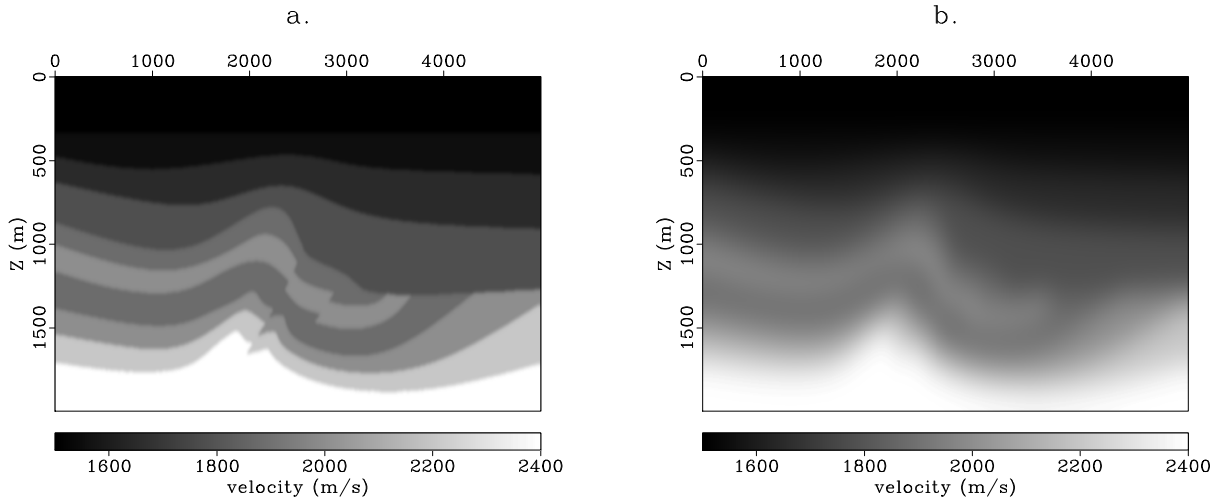

Figure 3 *Faulted velocity model* $[nx = 2000 \;\; nz = 800 \;\; \Delta x = 2.5m \;\; \Delta z = 2.5m]$, $\frac{V_p}{V_s} = \sqrt{2}$ *and density* $1000 - 1750\,kg/m^3$ *a.) Compressional velocities. b.) Smoothed compressional velocities used for wave-field extrapolation.*

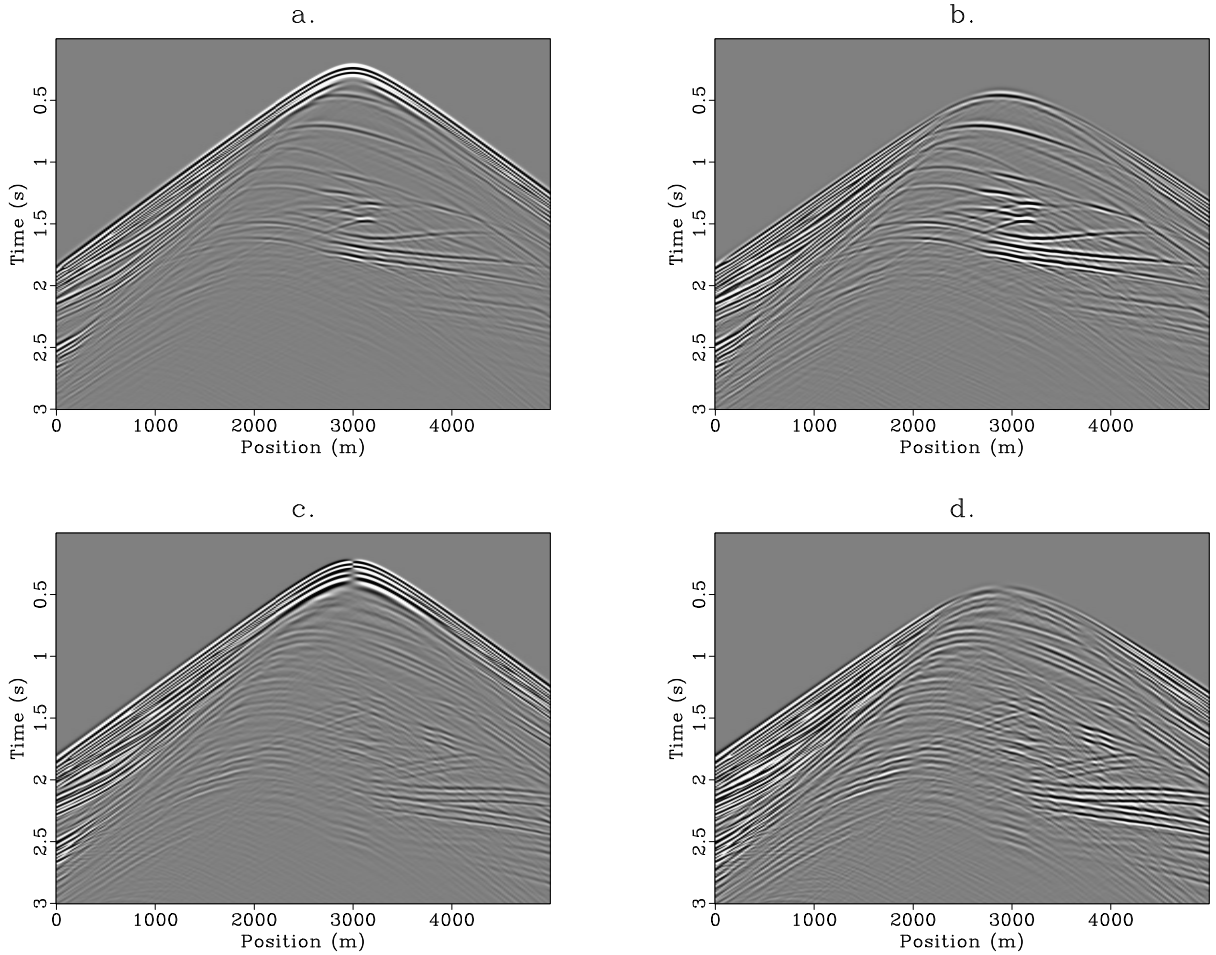

Figure 4 *Recorded data for* $3000\,m$ *shot. a.) Vertical particle velocity component* v_z*. b.)* v_z *with direct and scholte wave removed for back propagation. c.) Horizontal particle velocity component* v_x*. d.)* v_x *with direct and scholte wave removed for back propagation.*

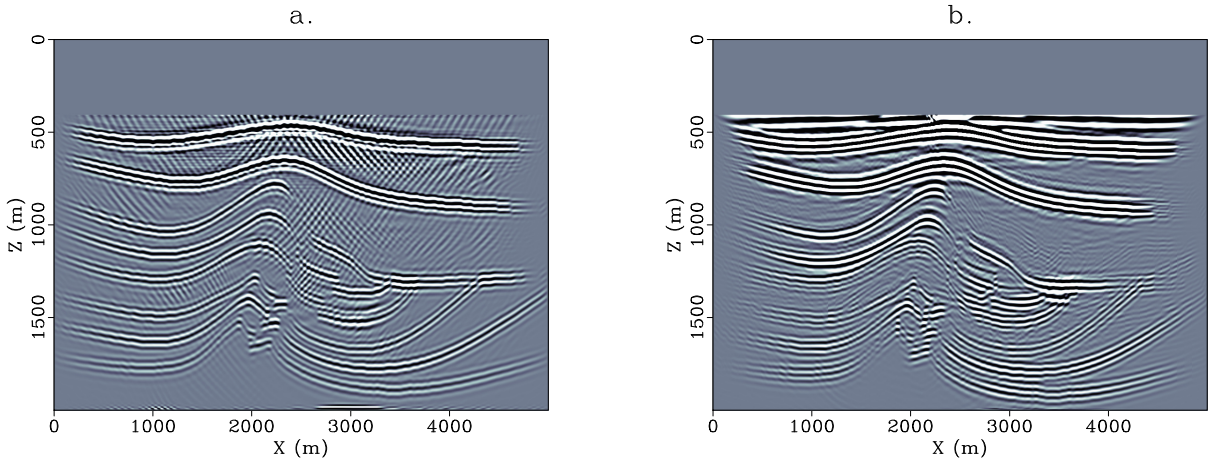

Figure 5 *64 Stacked partial images. The images are bandpass filtered and muted above the first reflector. a.) Migrated primary phases $F^{PP}(x,z)$. b.) Migrated converted phases $F^{PS}(x,z)$.*

Conclusions

Reverse time migration algorithms are a useful depth imaging tool when dealing with steeply dipping complex structure. We investigate a reverse time migration algorithm for two-dimensional isotropic elastic prestack data. The outlined Madariaga-Virieux staggered grid finite-difference scheme models seismic wave-field propagation. This finite-difference scheme acts as the engine of the reverse time migration algorithm extrapolating wave-fields forwards and backwards through time. A vector cross-correlation imaging condition then generates images for both primary and converted seismic phases. The method is applied to a faulted model OBN synthetic data set, and shows the ability to accurately resolve detailed images of subsurface impedance contrasts.

Acknowledgements

The authors would like to thank the sponsors of the Signal Analysis and Imaging Group (SAIG) at the University of Alberta, Madagascar open-source software package freely available from http://www.reproducibility.org, and Jinkun Cheng for construction of the velocity model.

References

Bayliss, A., K. Jordan, B. LeMesurier, and E. Turkel, 1986, A fourth-order accurate finite-difference scheme for the computation of elastic waves: Bulletin of the Seismological Society of America, **76**, 1115–1132.

Baysal, E., D. Kosloff, and J. Sherwood, 1983, Reverse time migration: Geophysics, **48**, 1514–1524.

Botelho, M. A., and P. L. Stoffa, 1991, Finite-difference prestack reverse time migration using the p-sv wave equation: Presented at the 1991 SEG Annual Meeting.

Chang, W., and G. McMechan, 1987, Elastic reverse-time migration: Geophysics, **52**, 1365–1375.

Chew, W., and Q. Liu, 1996, Perfectly matched layers for elastodynamics: A new absorbing boundary condition: Journal of Computational Acoustics, **4**, 341–359.

Claerbout, J. F., 1985, Imaging the earth's interior: Citeseer, **316**.

Collino, F., and C. Tsogka, 2001, Application of the perfectly matched absorbing layer model to the linear elastodynamic problem in anisotropic heterogeneous media: Geophysics, **66**, 294–307.

Dellinger, J., and J. Etgen, 1990, Wave-field separation in two-dimensional anisotropic media: Geophysics, **55**, 914–919.

Levander, A. R., 1988, Fourth-order finite-difference p-sv seismograms: Geophysics, **53**, 1425–1436.

Madariaga, R., 1976, Dynamics of an expanding circular fault: Bulletin of the Seismological Society of America, **66**, 639–666.

Sava, P., and S. Fomel, 2006, Generalized imaging conditions for wave-equation migration: Presented at the 68th EAGE Conference and Exhibition.

Sun, R., and G. A. McMechan, 2001, Scalar reverse-time depth migration of prestack elastic seismic data: Geophysics, **66**, 1519–1527.

Virieux, J., 1984, Sh-wave propagation in heterogeneous media: Velocity-stress finite-difference method: Geophysics, **49**, 1933–1942.

———, 1986, P-sv wave propagation in heterogeneous media: Velocity-stress finite-difference method: Geophysics, **51**, 889–901.

Whitmore, N. D., 1983, Iterative depth migration by backward time propagation: Presented at the 1983 SEG Annual Meeting, September 11 - 15, 1983 , Las Vegas, Nevada.

Yan, J., and P. Sava, 2008, Isotropic angle-domain elastic reverse-time migration: Geophysics, **73**, S229–S239.